

Review

Open Access

A review of common-path off-axis digital holography: towards high stable optical instrument manufacturing

Jiwei Zhang¹, Siqing Dai¹, Chaojie Ma¹, Teli Xi¹, Jianglei Di^{1*} and Jianlin Zhao^{1*}

Abstract

Digital holography possesses the advantages of wide-field, non-contact, precise, and dynamic measurements for the complex amplitude of object waves. Today, digital holography and its derivatives have been widely applied in interferometric measurements, three-dimensional imaging, and quantitative phase imaging, demonstrating significant potential in the material science, industry, and biomedical fields, among others. However, in conventional off-axis holographic experimental setups, the object and reference beams propagate in separated paths, resulting in low temporal stability and measurement sensitivity. By designing common-path configurations where the two interference beams share the same or similar paths, environmental disturbance to the two beams can be effectively compensated. Therefore, the temporal stability of the experimental setups for hologram recording can be significantly improved for time-lapsing measurements. In this review, we categorise the common-path models as lateral shearing, point diffraction, and other types based on the different approaches to generate the reference beam. Benefiting from compact features, common-path digital holography is extremely promising for the manufacture of highly stable optical measurement and imaging instruments in the future.

Introduction

Gabor invented holography in 1948, attempting to correct the spherical aberrations of the electron microscope¹. Based on Gabor's idea, the light field information including the amplitude and phase distributions could be retrieved by recording the interferogram of the object and reference waves. However, owing to the lack of highly coherent light sources and bottleneck of separating the twin images in the on-axis holography, holography did not receive serious attention at

that time. With the invention of the high coherence laser and proposal of off-axis holography², holography has since developed rapidly. However, limited by the complex physical and chemical processing of photographic plates or films, conventional holography has faced difficulties in real-time measurements. In 1967, Goodman introduced electronic-based imaging methods into hologram-recording and computer technologies into the image reconstruction³. Subsequently, digital holography was developed to realise the dynamic and quantitative measurement of different samples with high efficiency⁴. Based on diffraction theory, it was determined that the object light field could be numerically reconstructed using the digitally diffracted light wave from the digital hologram "illuminated" with a simulated reference light wave.

A potential problem of digital holography is that the

Correspondence: Jianglei Di (jiangleidi@nwpu.edu.cn) or Jianlin Zhao (jlzhao@nwpu.edu.cn)

Key Laboratory of Light Field Manipulation and Information Acquisition, Ministry of Industry and Information Technology, and Shaanxi Key Laboratory of Optical Information Technology, School of Physical Science and Technology, Northwestern Polytechnical University, Xi'an 710129, China

© The Author(s) 2021



Open Access This article is licensed under a Creative Commons Attribution 4.0 International License, which permits use, sharing, adaptation, distribution and reproduction in any medium or format, as long as you give appropriate credit to the original author(s) and the source, provide a link to the Creative Commons license, and indicate if changes were made. The images or other third party material in this article are included in the article's Creative Commons license, unless indicated otherwise in a credit line to the material. If material is not included in the article's Creative Commons license and your intended use is not permitted by statutory regulation or exceeds the permitted use, you will need to obtain permission directly from the copyright holder. To view a copy of this license, visit <http://creativecommons.org/licenses/by/4.0/>.

mismatch between the numerically simulated reference wave and experimentally used one could induce reconstruction errors such as phase aberration. Hence, different numerical methods were developed to address this problem⁵. Based on the double-exposure principle, digital holographic interferometry (DHI) can eliminate phase aberration through the phase subtraction of the object waves reconstructed by the holograms with and without the sample. Exploiting the capability of measuring physical parameters associated with the object wave phase, DHI has been applied to visualising different complex flow fields⁶ such as Karman vortex street in water flow⁷, temperature distribution of heat conduction process⁸, solution concentration variation⁹, liquid diffusion process¹⁰, sound pressure distribution¹¹, pulse laser ablation process¹², and sound waves¹³. In Fig. 1a–d, four examples are displayed.

In principle, the reconstructed object image can be numerically focused at any position¹⁶ for flexible microscopic imaging. Therefore, by combining digital holography with optical microscopy, digital holographic microscopy (DHM) has become a popular phase imaging method for semi-transparent and transparent (weak scattering) or reflective phase objects. Upon the reflection by the sample surface or transmission through the sample, the phase distribution of the probing beam carries the information of the sample's profile or refractive index (or thickness), respectively. Consequently, DHM enables high-contrast imaging of small specimens as well as quantitative

characterisation of the three-dimensional (3D) morphology and refractive index. Owing to the advantages of label-free, non-contact, and wide-field measurement, DHM and its derivatives have found wide application in industrial inspection, biomedical research, and other fields in the past decades¹⁷. However, the phase information obtained by DHM is an integral along the light propagation direction. To acquire the information inside the test specimen, digital holographic tomography (DHT) has achieved rapid progress and different approaches have been proposed to realise tomographic measurement^{14,15,18}. We display two application examples of DHT in Fig. 1e–k. In addition, 3D phase and fluorescence images have been simultaneously obtained using a coherent and incoherent integrated common-path DHM system¹⁹.

Another fundamental problem of digital holography is resolution improvement. Similar to other wide-field optical imaging modalities, the spatial resolution of digital holography is restricted by the spatial resolution of the imaging device and also obeys Abbe's diffraction limit²⁰. To improve the imaging resolution, numerous approaches such as oblique illumination^{21,22}, synthetic aperture^{23,24}, structured illumination²⁵, and speckle illumination²⁶ have been introduced²⁷. To further promote the application of digital holography, advanced computation techniques, for example, deep learning, have been introduced in digital holography for numerical reconstruction^{28–31}, fast image autofocusing^{32,33}, phase unwrapping³⁴, phase aberration

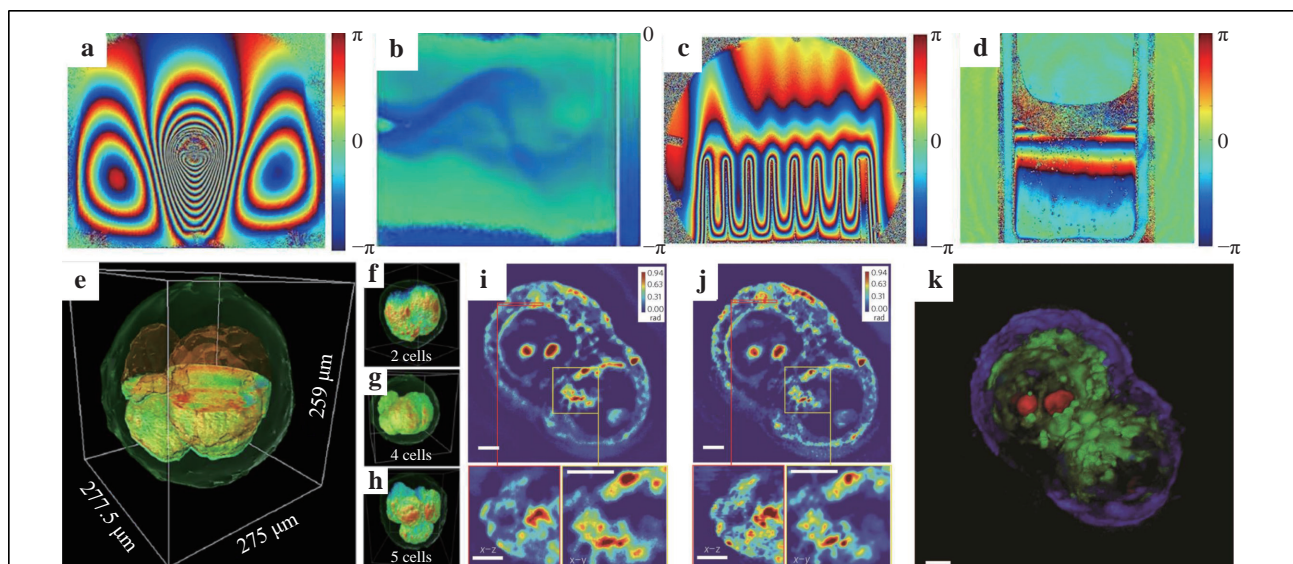


Fig. 1 Applications of DHI in visualising complex flow fields: **a** thermocapillary motion of a droplet⁶, **b** Karman vortex street⁷, **c** heat dissipation process of a heat sink⁸, and **d** protein-lysozyme solution crystallisation process⁹. Applications of DHT in 3D biomedical imaging: **e** an embryo cut through the centre and **f–h** different development stages of bovine embryos¹⁴. Measurement results of HT29 cells¹⁵: **i** Z-slice (top), cross-section of the region marked by the red box (bottom left) and enlargement of the region marked by the yellow box (bottom right), **j** deconvolved results of **i**, and **k** 3D rendering of the deconvolution result. Scale bars: 5 μm. Images reprinted with the following permissions: a⁶, b⁷, d⁹ from The Optical Society; c⁸ from AIP; e–k¹⁴ from Springer Nature.

compensation³⁵, and other uses. Deep learning has also been combined with digital holography to achieve additional functionality such as screening of anthrax spores³⁶, classification of cell morphology³⁷, and viral particle detection and classification³⁸.

Regarding the experimental configurations of digital holography and its derivatives, two basic types, namely in-line (on-axis, coaxial) and off-axis geometries are typically used. In-line geometry^{39–41} can fully use the camera bandwidth and phase shifting techniques can be used to remove the zero-order frequency component of the hologram⁴². To address the time-consuming problem in the phase-shifting operation, different parallel phase-shifting approaches have been developed^{43–46}. However, the corresponding experimental configurations are typically complex and not easily aligned. Therefore, off-axis geometry is more frequently considered, especially for practical instrument constructions. For traditional holographic interferometry, off-axis configurations based on Mach–Zehnder and Michelson interferometers are commonly established for (semi-) transparent and reflective test objects, respectively. Based on these two interference models, a Swiss company, Lyncée Tec SA (<https://www.lynceetec.com/>) pioneered the commercialisation of digital holographic microscopes and is leading this instrument industry. They have invented different types of microscopes that can be applied in dynamic topography, living cell imaging, MEMS testing, automated measurements, and other areas. Another company from the Republic of Korea, Tomocube (<http://www.tomocube.com/>), invented holotomographic microscopes based on the principle of DHT to measure the 3D refractive index distributions of biological cells and thin tissues. Our group has also been working on the instrumentation of off-axis holographic experimental setups, including instruments for measuring both large-size and microscopic objects. Fig. 2a–c are the transmission, reflection, and transmission and reflection integrated digital holographic microscopes invented by our group, respectively. Among these, the one

in Fig. 2c was built based on the mechanical structure of an inexpensive commercial microscope, making it easy to build and cost-effective.

In general, the object and reference beams in an off-axis holographic configuration interfere via separated paths to form the hologram. Consequently, any mechanical vibration or air disturbance, even marginal, can cause different influences on the two separated interference beams. This induces phase noise and results in low temporal stability. If the object and reference beams propagate along the same path in a common-path configuration⁴⁷, the environmental disturbance on the two interference beams can be effectively compensated with significantly enhanced temporal stability. In addition, the compact and robust common-path configuration is advantageous in optical instrument manufacturing. In this review, we summarise the design principle of the common-path off-axis digital holographic setups and present examples of their applications, providing a prospect in high stable optical instrument manufacturing.

Configuration design of common-path off-axis digital holography

First, we outline the basic principle of off-axis digital holography⁴⁸. As indicated in Fig. 3a, the object beam carrying the object information and reference beam, which is typically a uniform plane wave, interfere on the CCD camera with an appropriate angle. For simplicity, we assume that the object beam propagates along the y -axis and the optical axis of the reference beam has an angle of θ relative to the y -axis. The complex amplitudes of the two beams on the hologram-recording plane can be expressed as

$$e_o(x, y) = a_o(x, y) \exp[j\phi_o(x, y)] \quad (1)$$

$$e_r(x, y) = a_r(x, y) \exp\left(j2\pi \frac{\sin\theta}{\lambda} y\right) \quad (2)$$

where, $a_o(x, y)$ and $a_r(x, y)$ are the amplitudes and $\phi_o(x, y)$ is the phase distribution of the object wavefront. The

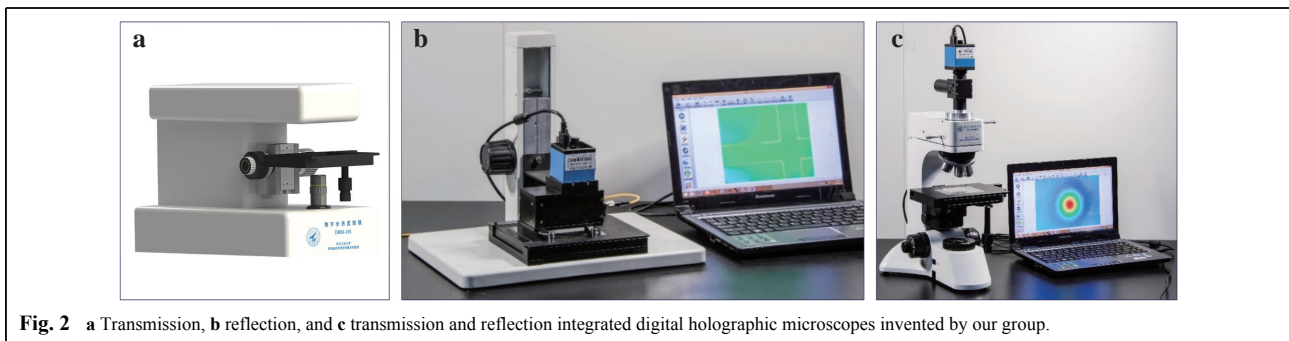
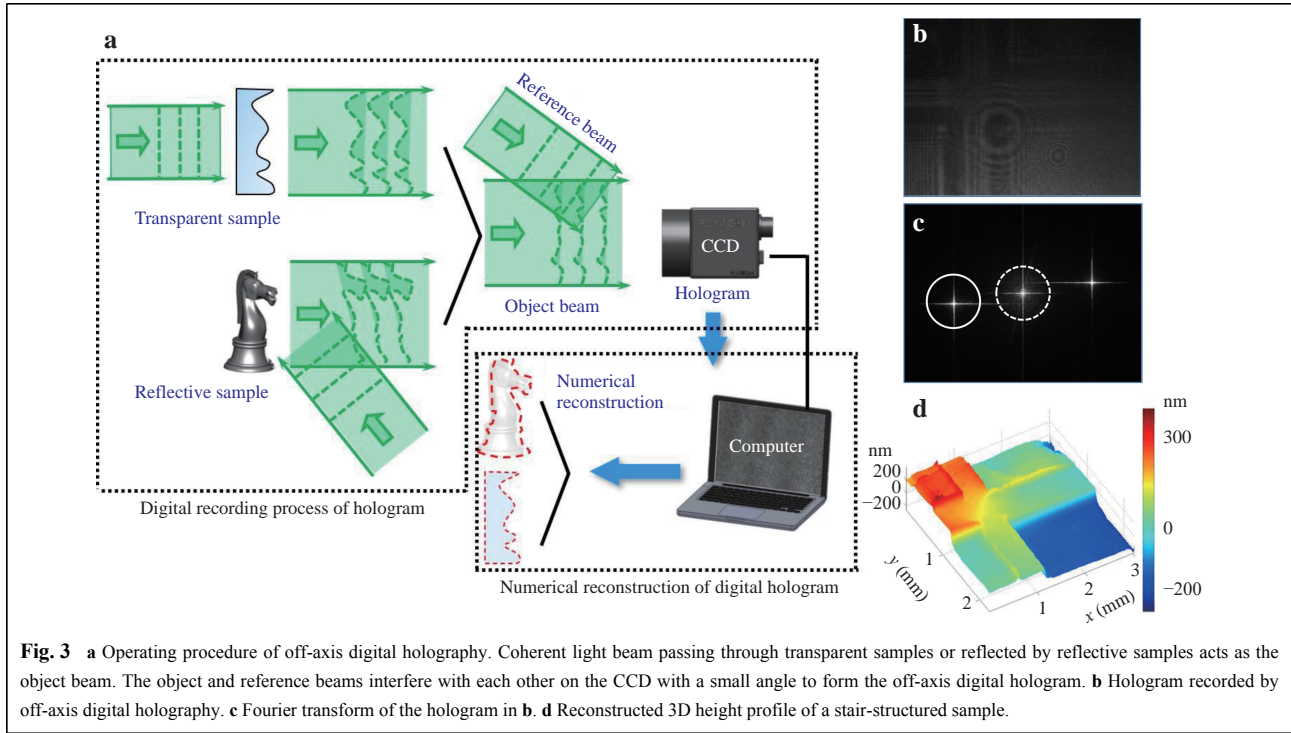


Fig. 2 a Transmission, b reflection, and c transmission and reflection integrated digital holographic microscopes invented by our group.



intensity distribution of the hologram, i.e., the interferogram between the two beams (see example in Fig. 3b) is

$$I(x, y) = |e_o(x, y) + e_r(x, y)|^2 = |e_o(x, y)|^2 + |e_r(x, y)|^2 + e_o(x, y)a_r^*(x, y)\exp\left(-j2\pi\frac{\sin\theta}{\lambda}y\right) + e_o^*(x, y)a_r(x, y)\exp\left(j2\pi\frac{\sin\theta}{\lambda}y\right) \quad (3)$$

For reconstruction, the conjugate of the original reference beam $e_r^*(x, y)$ is used to illuminate the hologram. The diffraction includes four parts:

$$U_1(x, y) = Te_r^*(x, y)|e_o(x, y)|^2 \quad (4a)$$

$$U_2(x, y) = Te_r^*(x, y)|e_r(x, y)|^2 \quad (4b)$$

$$U_3(x, y) = Te_r^*(x, y)e_o(x, y)a_r^*(x, y)\exp\left(-j2\pi\frac{\sin\theta}{\lambda}y\right) \quad (4c)$$

$$U_4(x, y) = Te_r^*(x, y)e_o^*(x, y)a_r(x, y)\exp\left(j2\pi\frac{\sin\theta}{\lambda}y\right) \quad (4d)$$

where T is the average transmission of the reconstruction wave passing through the hologram. Eq. 4a and 4b denote the 0th order diffraction components and Eq. 4c and 4d denote the separated twin images due to the carrier frequency of the reference beam. For numerical reconstruction of the object wave, the Fourier transform-based convolution method is typically used. The $\pm 1^{\text{st}}$ order

Fourier spectra of the hologram corresponding to Eq. 4c and 4d are separated in the Fourier space. The circles in Fig. 3c mark the 0th and 1st order Fourier spectra of the hologram in Fig. 3b. Because only the term in Eq. 4c contains the original object information $e_o(x, y)$, it can be reconstructed through properly selecting the 1st order spectral component in the Fourier space.

The complex amplitude of the diffraction wave carrying the object information at position $z = d$ from the hologram plane can be expressed as

$$u(\xi', \eta') = \int_{-\infty}^{\infty} \int_{-\infty}^{\infty} U_3(x, y)g_{\text{PSF}}(x - \xi', y - \eta') dx dy = U_3(x, y) * g_{\text{PSF}}(\xi', \eta') \quad (5)$$

where the symbol “*” denotes the convolution calculation and $g_{\text{PSF}}(\xi', \eta')$ is the point spread function (PSF), which can be expressed as

$$g_{\text{PSF}}(\xi', \eta') = \frac{j}{\lambda} \frac{\exp(-jk_0 \sqrt{d^2 + \xi'^2 + \eta'^2})}{\sqrt{d^2 + \xi'^2 + \eta'^2}} \quad (6)$$

Based on the convolution property of the Fourier transform, the reconstructed object wave can be expressed as

$$u(\xi', \eta') = F_{x,y}^{-1}[F_{x,y}(U_3)F_{x,y}(g_{\text{PSF}})] \equiv F_{x,y}^{-1}[F_{x,y}(U_3)G_{\text{PSF}}] \quad (7)$$

where the operations “ $F_{x,y}$ ” and “ $F_{x,y}^{-1}$ ” denote the two-dimensional Fourier transform and inverse Fourier transform, respectively, and G_{PSF} is the Fourier transform

of g_{PSF} and acts as the transfer function of the imaging system. Taking the discrete forms, the reconstruction can be performed digitally. Fig. 3d displays the calculated 3D height profile of a stair-structured sample from the hologram in Fig. 3b.

To record the off-axis hologram, the object beam must interfere with a uniform reference beam at a certain angle. The key issue to design a common-path configuration is to generate a uniform reference beam allowing the two interference beams to pass along similar paths. The greater the level of similarity, the greater the stability of the optical setup. From the perspective of the approach to generate the reference beam, we categorise the common-path models as lateral shearing, point diffraction, and other types.

Common-path configuration based on lateral shearing

The lateral shearing interferometer was invented to measure the asphericity of an optical wavefront⁴⁹. The wavefront under test is first doubled using specific optical elements and the two wavefronts create a lateral shear or displacement. The overlapping area of the two wavefronts forms the interferogram for further analysis. The two wavefronts propagate along similar paths, which inspires the design of lateral shearing-based common-path configurations for off-axis digital holography. The concept of lateral shearing-based off-axis digital holography is illustrated in Fig. 4. The illumination beam passes through a (semi-) transparent sample (or is reflected by an opaque sample) and an imaging system. A beam duplicator reproduces the beam into two beams that are projected on the CCD target at a proper angle. Note here that both beams carry the same sample information. However, as discussed in the previous section, a uniform reference beam containing no sample information is required for the hologram formation. Therefore, the test sample in the lateral shearing-based common-path configuration must be sparse in the field of view (FOV), or only a portion of the beam illuminates the sample. In this manner, the effective

interference area, i.e., the overlapping area of the two beams with and without the sample information, can be realised. This feature is different from that of a traditional lateral shearing interferometer.

Using a glass plate

Multiple optical components such as glass plate^{50–53}, grating^{54–58}, and beam splitter (BS)^{59–62} are typically employed as the beam duplicator in the lateral shearing-based common-path configurations. Fig. 5 displays an example using a glass plate⁵⁰. A plane wave passing through the sample is expanded by a microscope objective (MO) to become a divergent beam. The beam is then reflected at the front and back surfaces of a glass plate oriented at approximately 45° relative to the optical axis of the beam. Consequently, the incident beam is doubled to create a lateral shearing, as indicated in Fig. 5(a). The two beams are divergent satisfying the recording condition of the off-axis geometry. This configuration can be easily integrated with a commercial microscope for practical applications. Glass microspheres were used as the test samples. The hologram was recorded when only one sphere appeared in the FOV. The height of the sphere surface $d = \phi\lambda / (2\pi\Delta n)$ was retrieved from the phase image, where ϕ is the phase value, λ is the light wavelength, and Δn is the index difference between the sample and its surrounding media. Fig. 5b displays the retrieved height distribution of the sphere surface. Note here that the seemingly “two” spheres with positive and negative heights are displayed in the image. In fact, it represents the information of the same sphere. Two spheres appear in the FOV because the beam is reflected twice by the glass plate, and the bending direction of the interference fringes of the left sphere is opposite to that of the right sphere. The duplicated image can limit the effective FOV of this experimental setup. To address this problem, the illumination beam size must be sufficiently large such that the object size is smaller than the interference area and only one copy of the object information is imaged onto the CCD target. Fig. 5c displays the 3D height profile of the

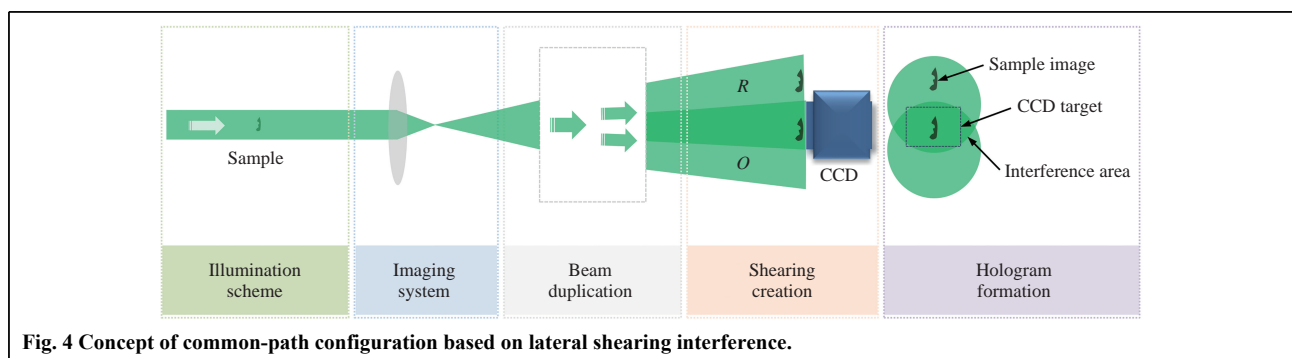
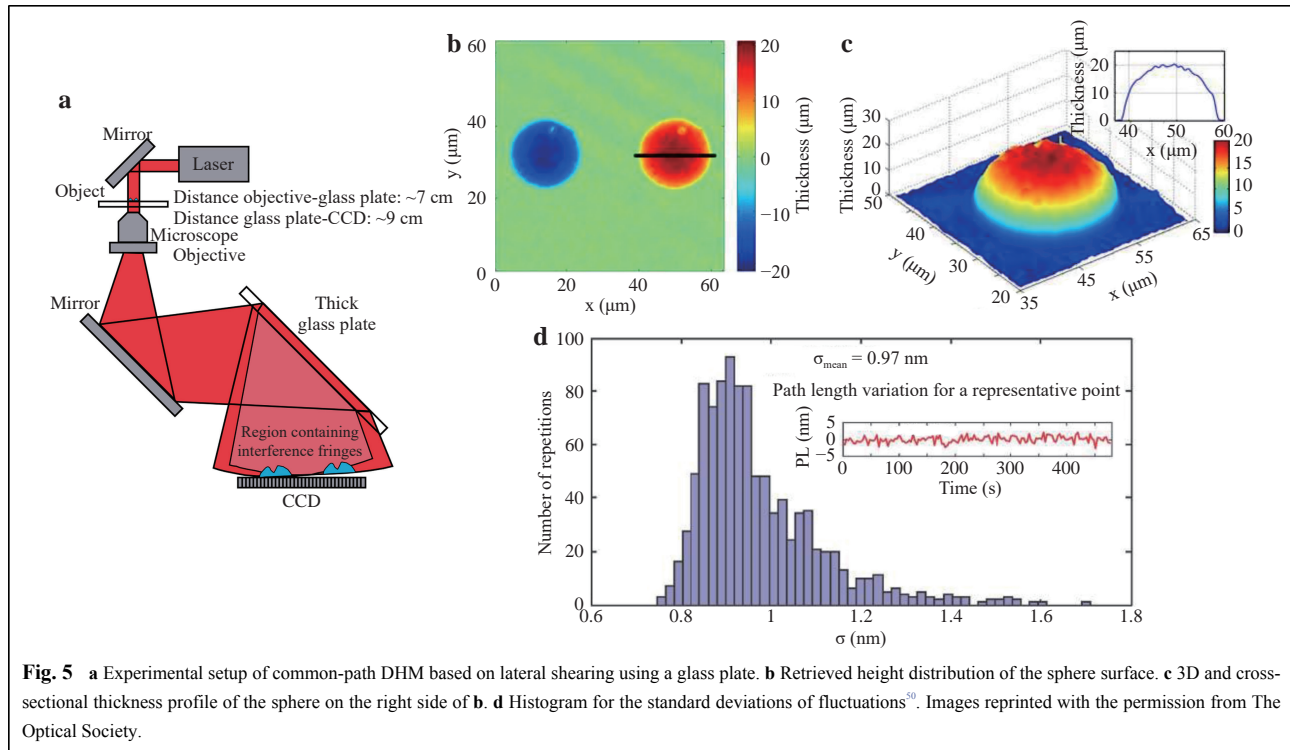


Fig. 4 Concept of common-path configuration based on lateral shearing interference.



sphere surface on the right side of Fig. 5b, and the inset indicates the corresponding cross-sectional profile.

The common-path holographic configuration can improve the temporal stability of the setup, especially the phase measurement stability of the object wave. The stability characterisation should be performed without vibration compensation. Using the setup in Fig. 5a as an example, 1200 holograms without objects were recorded over an area of $37.5 \mu\text{m} \times 37.5 \mu\text{m}$ at a speed of 2.5 frames per second for 8 minutes. Phase images of all the holograms were reconstructed and the optical path difference was obtained by subtracting the phase values with that of the previously recorded hologram. Then, 1024 pixel positions were randomly selected in the FOV and the standard deviations of the fluctuations of these positions were calculated. Fig. 5d displays the histogram of the fluctuations with an average value less than 1 nm at a wavelength of 632.8 nm. This indicates an optical path fluctuation of only 0.01 rad. This small fluctuation demonstrates the high temporal stability of the experimental setup.

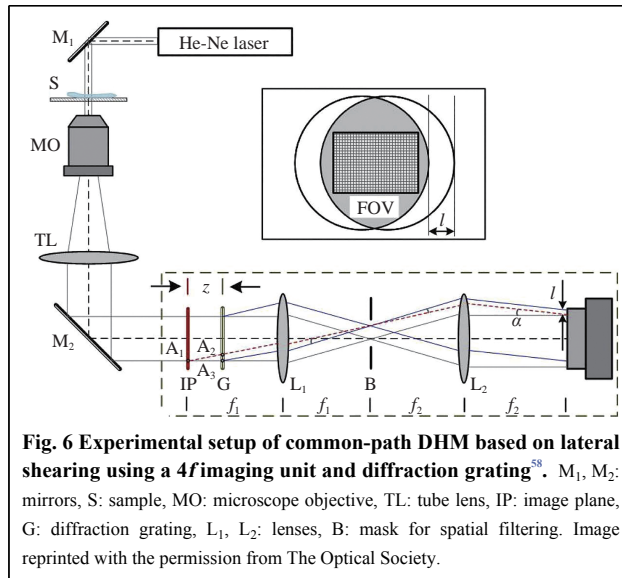
Based on the lateral shearing-based common-path configuration using a glass plate, researchers developed a compact structured-illumination-based DHM setup⁵³. By illuminating the sample with structured intensity patterns, the imaging resolution of the amplitude- and phase-contrast images can be effectively enhanced. This design reduces

the complexity of the setup and provides high temporal stability.

Using a grating

In the previous glass plate-based configuration, the divergent beam from the MO reaches the CCD target without an imaging lens. The object cannot be directly imaged on the hologram-recording plane and thus it needs to set an appropriate reconstruction distance. To record the image plane hologram, alternative optical components can be employed. Fig. 6 displays an example of using a grating as the beam duplicator⁵⁸. A plane wave illuminates the sample. The transmitted beam is expanded by an MO and then passes through an imaging tube lens TL, by which the sample is imaged on the image plane IP. A grating G is placed at a distance z after the IP to reproduce multiple replicas of the sample image. Then, the intermediate sample images are projected onto the camera target *via* a $4f$ unit with lenses L_1 and L_2 . During this process, a mask B for spatial filtering is placed at the Fourier plane of lens L_1 , such that only the 0th and +1st diffraction orders can pass through it. These two orders are Fourier transformed again by lens L_2 to produce lateral shearing interference (shearing distance l) and form an off-axis image plane hologram. This lateral shearing module can also be integrated with a commercial inverted microscope.

In general, there is a tradeoff between the FOV and off-axis angle that should be balanced in practical applications.



Conversely, in the common-path configuration of Fig. 6, the off-axis angle is solely determined by the grating period d and focal lengths of lenses L_1 and L_2 , i.e., $\alpha = f_1 \lambda / f_2 d$. The shearing distance $l = f_2 \lambda z / f_1 d$ is dependent on the distance z , which can be adjusted by moving the grating along the optical axis freely. Consequently, the off-axis angle related to the interference fringe frequency is not required to match the shearing distance. The flexible selection of the shearing distance does not lose the spatial frequency of the sample.

In addition to the one-dimensional grating, a specific two-dimensional grating has been applied to create four replicas of the object image. Combining the setup in Fig. 6 with multiplexing techniques, researchers have recorded a polarisation hologram and reconstructed the wavefronts of two orthogonally polarised components containing the sample information using a single camera shot^{55,51}.

Using a BS

A single BS can also be employed to construct lateral shearing-based common-path DHM configurations^{59–62}. The output beam from a microscopic imaging system contains the half-object and half-reference parts. Then, the entire beam is further divided by a BS to create the sheared beams. Finally, the half-object and half-reference beams interfere with each other at a certain angle. Using the setup in Fig. 7a, which uses a slight trapezoid Sagnac interferometer and was developed by our group⁶⁰ as an example, a polarised BS (PBS) splits the object beam into two counter-propagating components with orthogonal polarisation states. The two components pass through the identical optical elements and then reach the CCD target. The off-axis recording condition can be achieved by marginally rotating the PBS with the transmitted p -

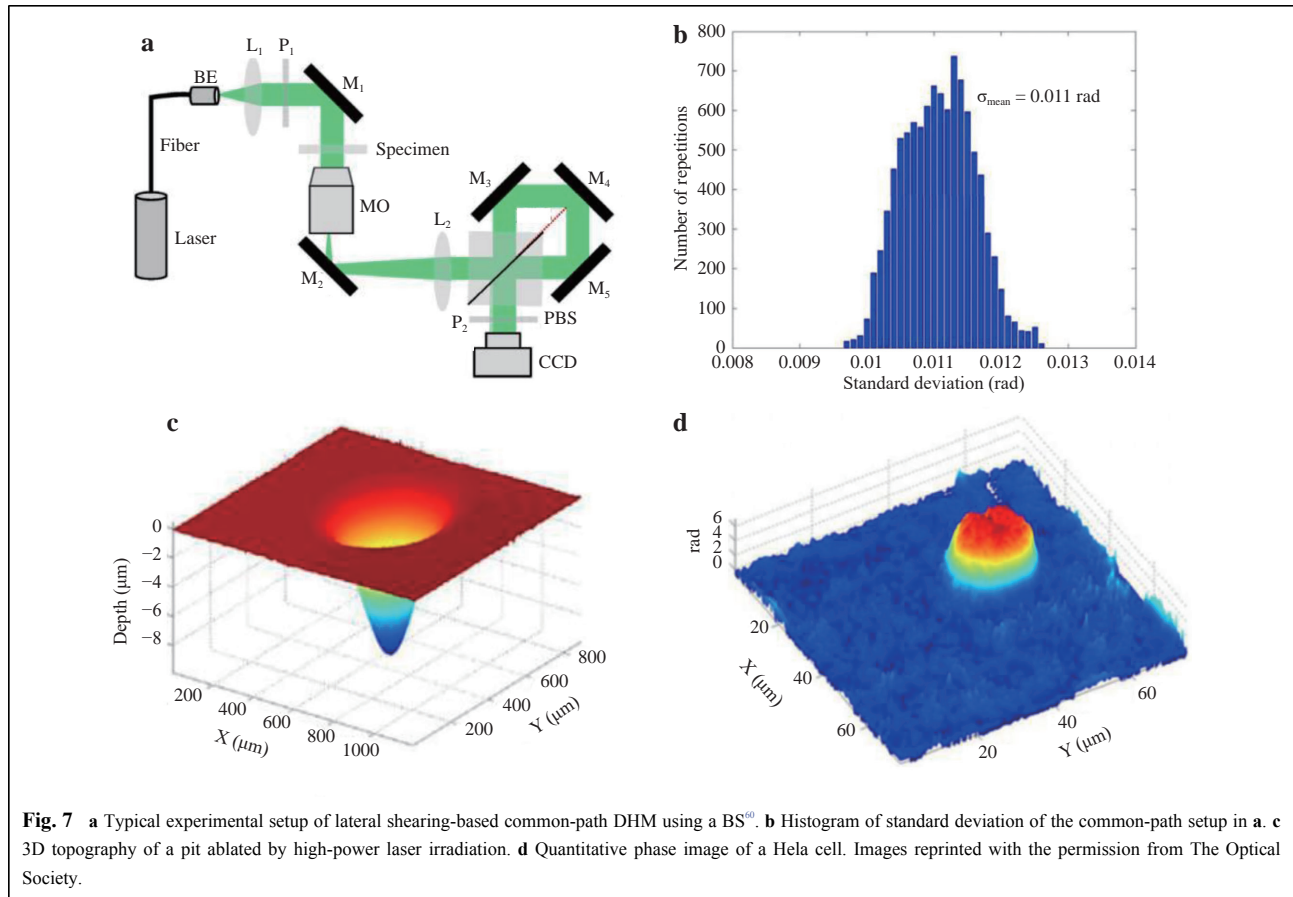
polarised component maintaining the propagation direction perpendicular to the CCD target. Consequently, the p -polarised component acts as the object beam, whereas the s -polarised component contains no sample information and serves as the reference beam. A polariser P_2 is used before the CCD to modulate the fringe contrast of the hologram. Note that the functionality of the BS used here is different from that in the Mach–Zehnder and Michelson interferometer-based setups. The two interference beams in Fig. 7a pass along the same paths, ensuring the high temporal stability in the configuration. To verify its high temporal stability compared with that of a Mach–Zehnder interferometer-based configuration, a similar characterisation method with that of Fig. 5d was used. The results demonstrated that the mean phase fluctuation of the common-path setup and Mach–Zehnder interferometer was 0.011 rad (Fig. 7b) and 0.106 rad, respectively. That is, the temporal stability of this common-path configuration was approximately one order of magnitude greater than that of the uncommon-path interferometer configuration. Owing to the high stability, we monitored a water evaporation process that has wide application in microfluidics, surface self-cleaning, and other areas⁶³. Moreover, two static measurements were also experimentally demonstrated. The first was a pit on a silica glass damaged by high-power laser irradiation. The retrieved pit depth is displayed in Fig. 7c. The other was a living Hela cell, which is in the human cervical cancer cell lines. The reconstructed quantitative phase image of the cell is displayed in Fig. 7d.

Other special optical components such as beam displacer⁶⁴, Wollaston prism (WP)⁶⁵, Rochon polariser⁶⁶, gradient-index lens⁶⁷, and biprism⁶⁸ can also be utilised in the lateral shearing-based common-path configurations to construct compact and stable holographic experimental setups.

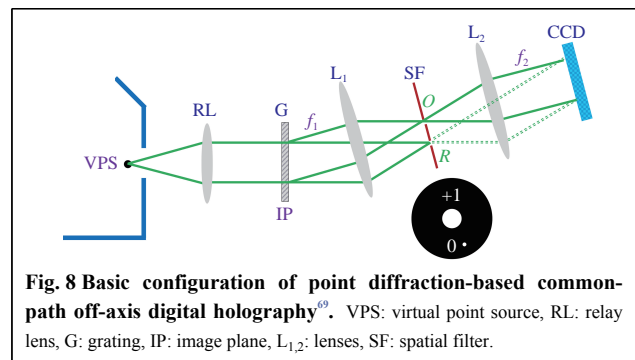
Common-path configuration based on point diffraction

In the lateral shearing-based common-path off-axis holographic experimental setups, sparse samples in the FOV or undisturbed portion of the illumination beam are required. Moreover, it has a potential problem of a duplicated image appearing on the camera target if the shearing distance is not sufficiently large, which could limit its practical applications. Alternatively, another common-path model referred as diffraction phase microscopy (DPM) was developed by Gabriel⁶⁹.

As discussed in the previous section, the key issue to design a common-path configuration is to generate a uniform reference beam allowing the two interference beams to propagate along the same or similar paths. Here,



we introduce the principle of generating the reference beam using the point diffraction model. As depicted in Fig. 8⁶⁹, a magnified sample image is obtained in an inverted microscope. To illustrate the imaging process, we start from a virtual point source (VPS) representing the object plane. At the image plane (IP), a grating G replicates the microscopic image and generates several diffraction orders. Then, the diffractions enter into a $4f$ unit with lenses L_1 and L_2 . The 0th order beam is low-pass filtered by a pinhole at the focal plane of L_1 , resulting in a uniform reference beam. Simultaneously, one of the 1st order beams containing complete sample information passes through the unit and becomes the object beam. Finally, the two beams interfere with each other on the CCD target at an appropriate off-axis angle. As this common-path configuration generates the uniform reference beam by diffracting the object beam through a “point” pinhole, we call this model the “point diffraction model”. Unlike the typical Mach–Zender interferometer, here the interference beams pass through the identical optical elements, ensuring high temporal stability. The average standard deviation of the optical path length in the full FOV was measured as 0.7 nm at a wavelength of 532 nm and the temporal



standard deviation was 0.04 nm⁶⁹. Similar to the lateral shearing-based common-path configurations, the common-path module in Fig. 8 can also be integrated with a commercial microscope.

Laser-based illumination

The module in Fig. 8 using a grating for beam duplication, however, has a low utilisation efficiency of the light power and is also somewhat bulky as a $4f$ unit is included. Hence, alternative designs have been proposed to realise the point diffraction^{70–72}. For example, a so-called τ interferometer is mounted at the output port of a

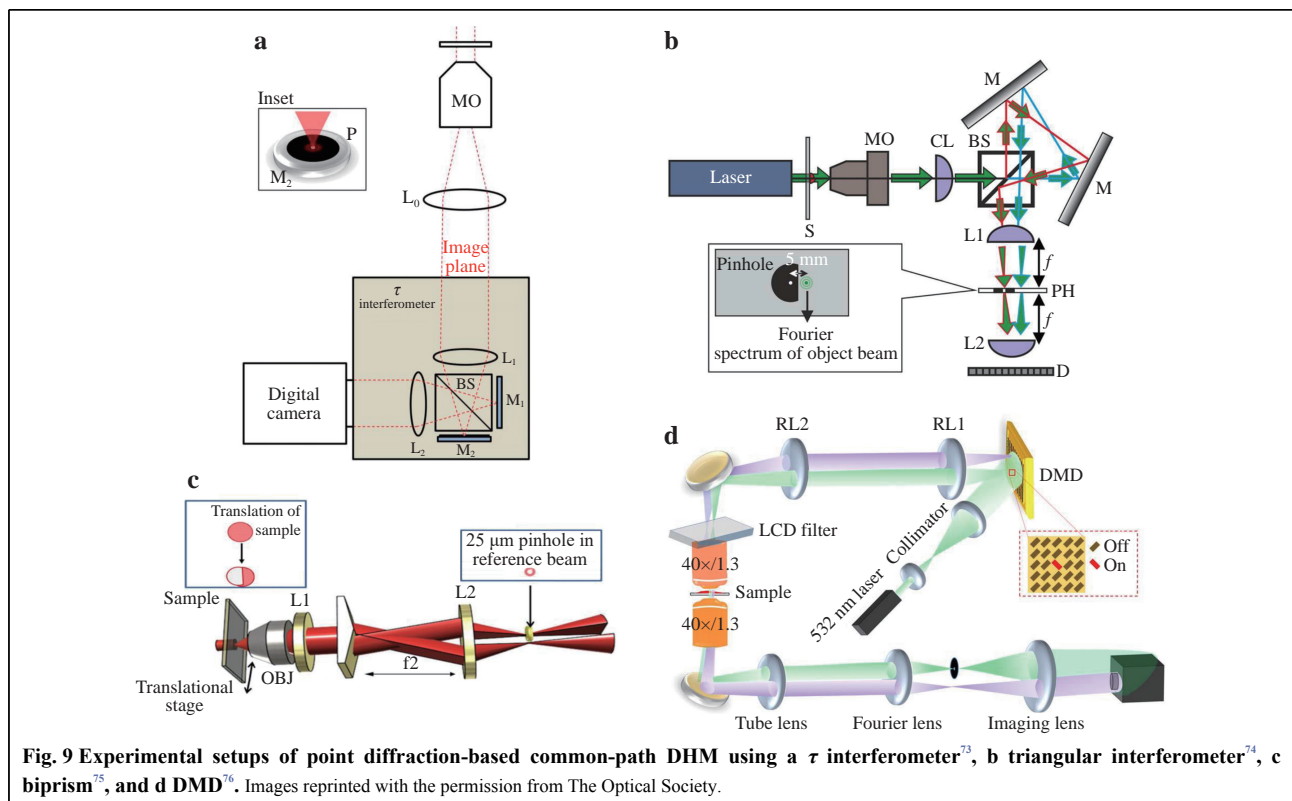
microscope (Fig. 9a)⁷³. This interferometer reproduces the object beam using a cubic BS and two mirrors reflect the beams. The pinhole is pasted on one of the mirrors to eliminate the sample information and create a uniform reference beam. The triangular interferometer-based setup in Fig. 9(b) also uses a cubic BS for the beam duplication, however, the pinhole is implemented in the transmission mode⁷⁴. A biprism can effectively double the object beam, not only compatible in the lateral shearing-based but also in the point diffraction-based common-path configurations (Fig. 9c)⁷⁵. Unlike the former configurations, a digital micromirror device (DMD)-based setup reproduces the uniform beam before passing through the sample, as depicted in Fig. 9d⁷⁶. A DMD positioned at the conjugate plane of the MO's back-aperture plane generates two plane waves for the illumination. Moreover, a glass plate, typically used in a lateral shearing-based configuration with a limited FOV, can also reproduce the object beam in the point diffraction-based configuration with high utilisation efficiency of the light power⁷⁷.

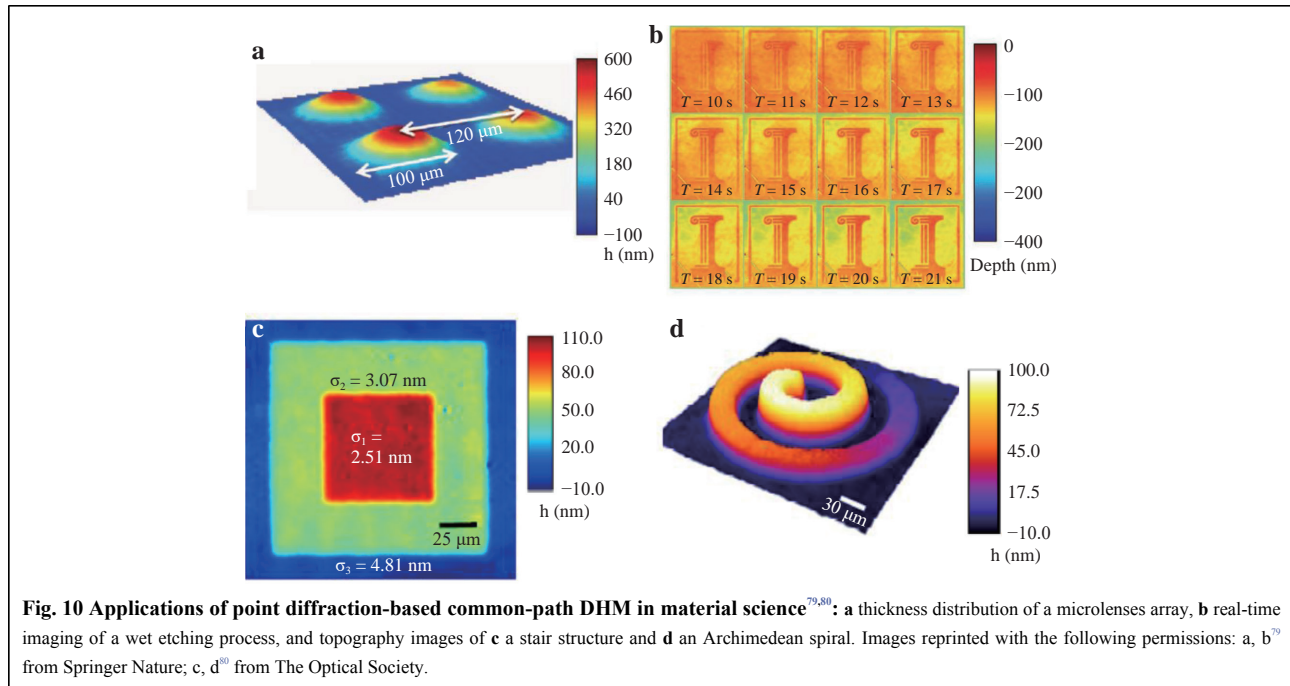
Owing to the high stability and compact features, the point diffraction-based common-path DHM has been widely used in biological studies, material science applications, and other applications⁷⁸. For example, the thickness distribution of a 2×2 array of microlenses was measured, as displayed in Fig. 10a. In addition, researchers

have constructed a DHM setup that operates in reflection mode for opaque samples and dynamically monitored nanoscale topographic changes during semiconductor etching. Fig. 10b displays the reconstructed logo of the University of Illinois when a GaAs wafer was being etched with a solution⁷⁹. Fig. 10c and 10d present the measured topography images of a multi-step stair structure and Archimedean spiral, respectively⁸⁰.

White light illumination

Speckle noise caused by the high coherence of lasers can typically contaminate reconstructed object images, resulting in a decrease of the phase measurement sensitivity and limiting the capabilities of investigating samples with subcellular features. Hence, white light illumination with low coherence is applied in point diffraction-based common-path DHM to decrease the spatiotemporal noise effectively^{15,81,82}. The corresponding setup is developed from that in Fig. 8, as indicated in Fig. 11a⁸². One of the differences is that a low-coherent halogen lamp with a condenser is used for the illumination. By closing down the condenser aperture to the minimum, the entire illumination field is spatially coherent. Another difference is that digital masks on a spatial light modulator (SLM) perform the spatial filtering to generate the object and reference beams. This common-path configuration makes the optical path difference between the object and





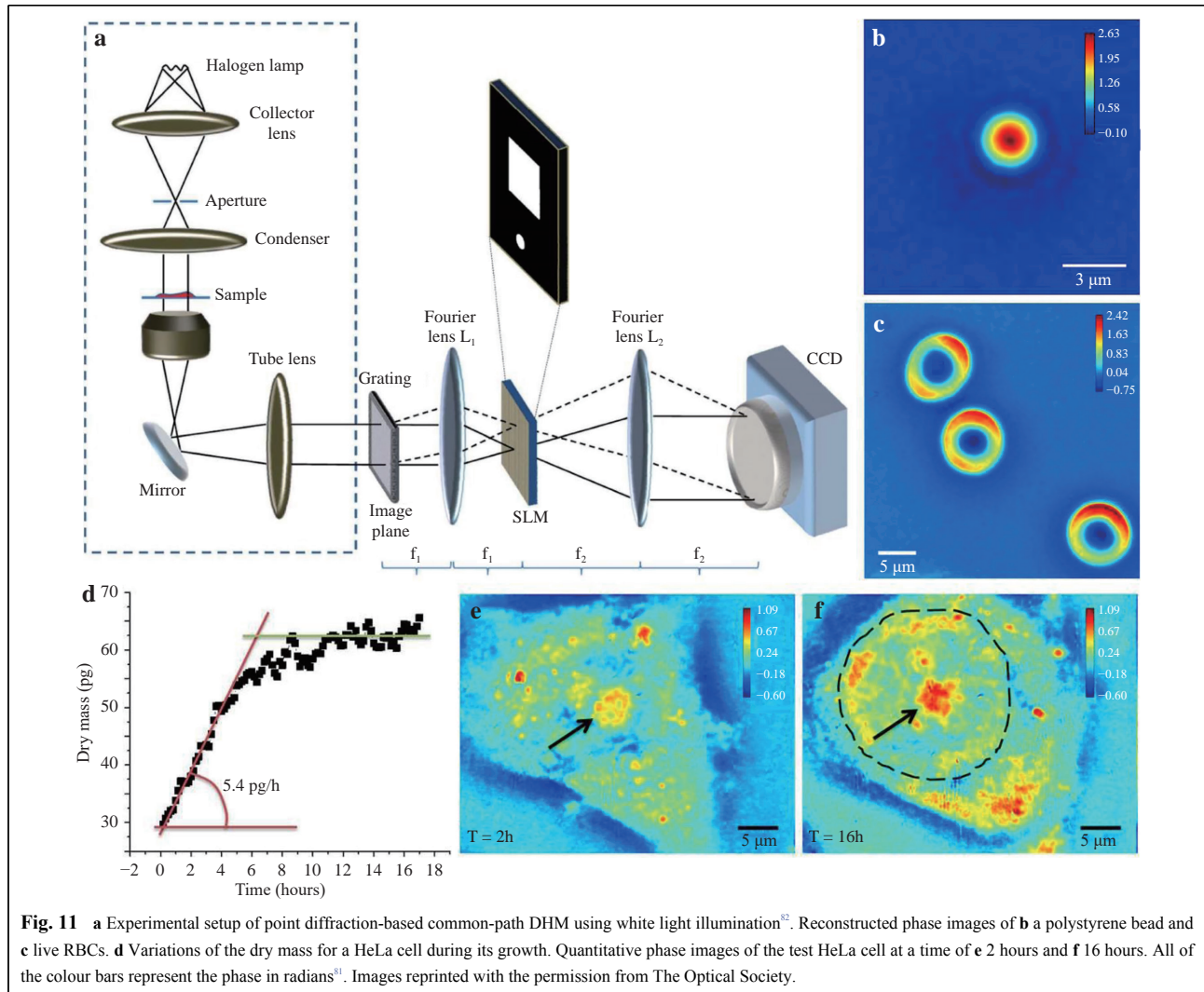
reference beams extremely small, such that the two beams are coherent and can interfere with each other regardless of the wavelength used. In addition to the SLM, a liquid crystal display device has also been applied to provide the digital filter masks⁸³.

The white light illumination-based setup exhibits high temporal stability owing to the common-path configuration and high phase measurement sensitivity due to the low-coherent illumination. It has found wide applications in the biomedical field including red blood cell (RBC) membrane fluctuation measurement⁸¹, cardiomyocyte cell beating measurement, and cell growth study⁸⁴. In the following, we provide application examples. Fig. 11b displays the reconstructed phase image of a polystyrene bead. Fig. 11c displays the phase image of three live RBCs where the typical discocyte shapes are clearly present. It can be observed that the phase background of the image is considerably uniform owing to the low coherent illumination. Moreover, the growth of Hela cells was monitored. The dots in Fig. 11d indicate the variations of the cell's dry mass with time. It can be observed that the test cell grows rapidly in the first six hours. Then, its growth slows and finally saturates. Fig. 11e–f are the phase images of the test cell at a time of 2 hours and 16 hours, respectively. As indicated by the arrows, the cell nucleolus in Fig. 11f is becoming larger than that in Fig. 11e.

Regardless of whether the illumination is laser-based or white light-based, each type has its advantages and disadvantages. It was found that laser-based illumination is

superior for material science applications where the samples have fine structural features or sharp edges. Conversely, white light-based illumination is more advantageous in biological applications where the sample features are smooth. Moreover, researchers have recently developed an endoscopic phase microscope⁸⁵ that combines a gradient-index-lens-based endoscope probe with a point diffraction-based common-path module, and allows single-cell-level resolution phase imaging. This instrument has broadened the application fields of quantitative phase imaging and has demonstrated significant potential in on-site studies.

The common-path configurations discussed above use a single laser or white light source, which cannot attain the distribution of a spectroscopic object light field. However, in transmission DHM, the measured phase information of the sample is proportional to the optical thickness, which is the integral product of the sample thickness and index. Owing to this dual dependence, the thickness and index information of the sample is ambiguous. Hence, more than one measurement is required to decouple these two physical parameters. By performing two measurements with different surrounding media, the thickness and index of the sample could be retrieved through a decoupling procedure⁸⁶. However, the sample state could be disturbed if the surrounding medium is changed. Alternatively, measuring phases of the object wave at different wavelengths can address this problem based on the dispersion property of the surrounding medium⁸⁷. For



example, spectroscopic phase microscopy has been introduced in point diffraction-based common-path DHM configurations^{88–90}.

Other common-path configurations

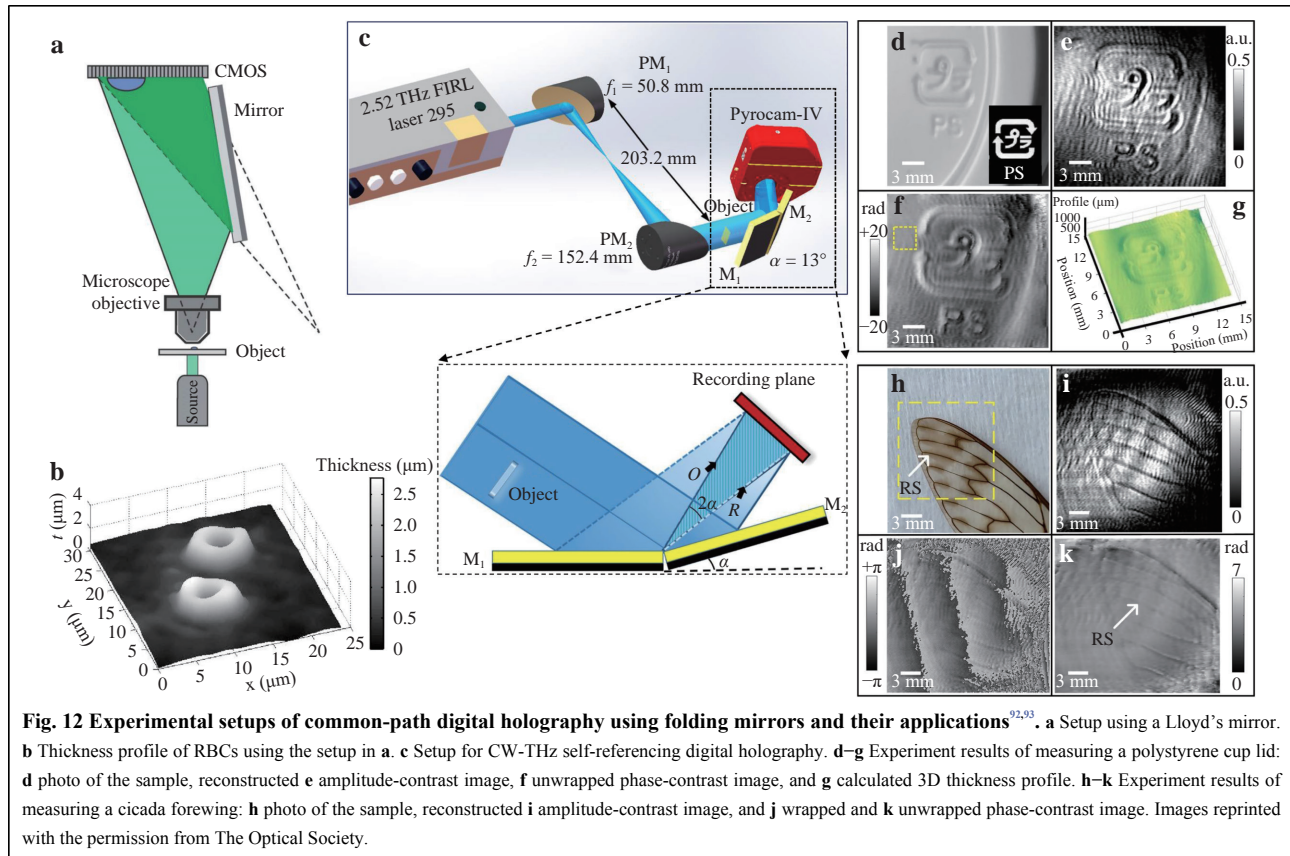
Apart from the two types discussed above, other advanced designs have also been proposed to construct common-path off-axis holographic experimental setups⁹¹.

Using a folding mirror

One example uses a self-referencing Lloyd's mirror configuration. As indicated in Fig. 12a, the laser beam passing through the sample is first expanded via an MO. Then, a mirror folds a part of the divergent beam onto the CMOS target. The straight propagating beam carrying the object information and unperturbed reflection beam interfere with each other to form the off-axis hologram⁹². This DHM setup is compact, portable, stable, and easy to implement. Its temporal stability was measured to be

approximately 0.9 nm without any vibration compensation, making it suitable for monitoring the changes of a cell profile. Fig. 12b displays an experiment result of the thickness profile of RBCs.

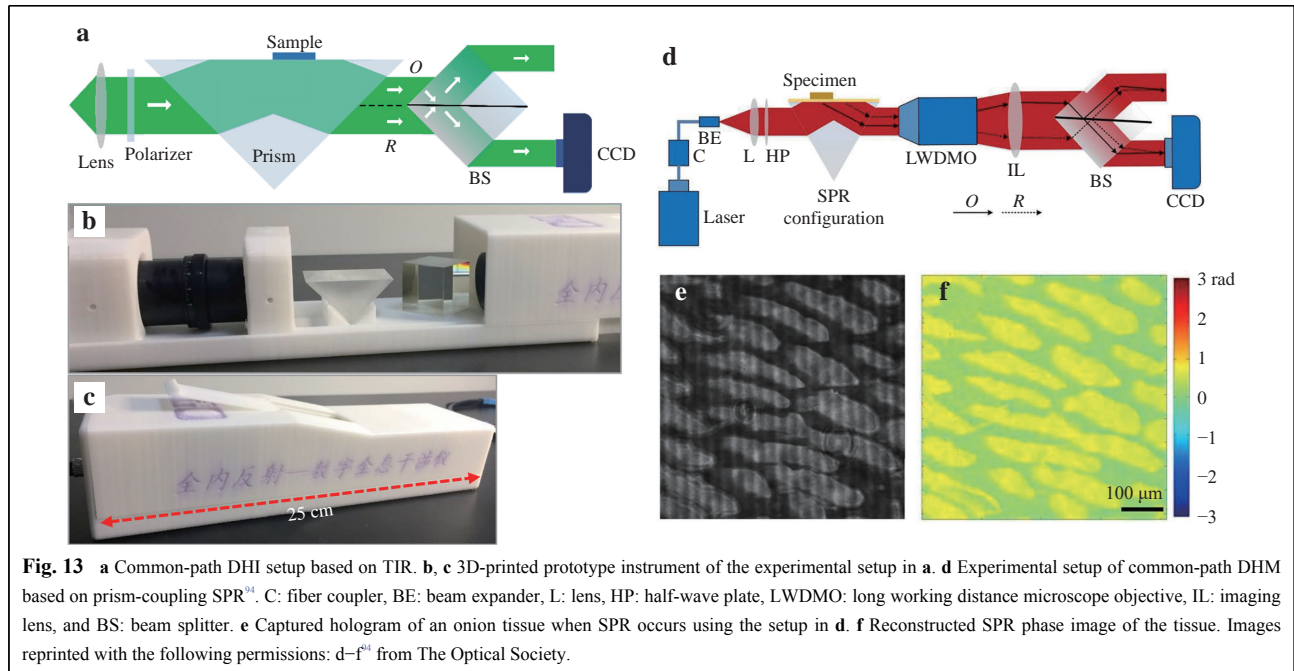
Fig. 12c displays a similar design applied in continuous-wave terahertz (CW-THz) holography⁹³. The inset indicates that the sample is illuminated by a half part of the terahertz wave. A pair of mirrors (M_1 and M_2) with an angle of α reflect the entire wavefront into two beams with an angle of 2α . Because the two beams are created from the same wavefront, their power and path length are virtually the same, forming interference patterns with high contrast. Unlike digital holography with visible light illumination, terahertz digital holography is a viable candidate for measuring optically opaque samples. Using the common-path setup in Fig. 12c, a polystyrene cup lid and biological samples such as insect wings are measured. The experiment results are presented in Fig. 12d–g and 12h–k, respectively.



Using a specially positioned BS cube

Another example uses a single BS cube positioned in a special manner^{94–96}. Fig. 13a presents an experimental setup of DHI based on total internal reflection (TIR)⁹⁷ to dynamically measure the refractive index distribution of liquid samples. The sample is located at a half part of the prism surface. Only one portion of the reflected beam carries the sample information, the other acts as the reference beam. The entire beam is incident on a BS cube with the semi-reflecting layer marginally inclined relative to the optical axis. The object beam transmits through the layer and the reference beam is reflected. The off-axis angle of the two interference beams is controlled by rotating the BS. The usage of a single BS cube creates a symmetrical common-path configuration. The spherical phase curvature of the illumination beam can be compensated physically by the reference beam during the interference. Owing to the advantages of this common-path holographic configuration, we built a prototype instrument of this setup using the 3D printing technology, as displayed in Fig. 13b–c. This instrument is compact with a total physical length of only 25 mm (Fig. 13c). More importantly, it possesses high measurement stability for on-site applications.

Furthermore, we applied an MO with a long working distance (LWDMO) in the BS cube-based DHM for surface plasmon resonance (SPR) imaging^{94,95}. As indicated in Fig. 13d⁹⁴, a *p*-polarised beam is reflected at the interface of an SPR configuration consisting of a prism, thin metal film, and dielectric layer. When the incident angle is greater than the critical angle of the TIR, the evanescent wave penetrates from the prism into the metal film. Once the wave vectors of the evanescent wave and surface plasmon wave match with each other at a certain angle, SPR occurs. The test sample acting as the dielectric layer is located at a half part of the metal film, which is the same with that in the setup displayed in Fig. 13a. Then, the entire beam is magnified by the LWDMO and passes through an imaging lens. Subsequently, the beam enters into the BS cube-based common-path configuration. The proposed common-path holographic experimental setup based on SPR (SPRHM) has advanced configuration simplicity as it contains fewer optical components. Moreover, high temporal stability can be realised to achieve highly sensitive SPR measurements. Using the setup in Fig. 13d, we performed SPR imaging of an onion tissue. The captured hologram in Fig. 13e indicates that the cell structures are clearly presented owing to the high



sensitivity of SPR. The reconstructed phase image in Fig. 13f has a high contrast. Owing to the high sensitivity of SPR and high stability of the common-path configuration, the SPRHM setup in Fig. 13d can image samples with low-contrast index distribution.

Using a WP

The previous common-path SPRHM setup uses a prism-coupling configuration for SPR excitation. Typically, to realise high-resolution SPR imaging, MOs with high magnification and numerical aperture (NA) are required after the prism. However, the working distance of this kind of MO is typically short and incompatible with the prism-coupling SPR configuration because of the geometry limitation of the prism. Furthermore, the direction of the reflected light changes as the SPR excitation angle varies, which requires the realignment of the experimental setup. For this reason, another common-path SPRHM setup based on the MO-coupling configuration was developed⁹⁸ using an immersion MO with NA greater than the one for SPR excitation.

As exhibited in Fig. 14a, a focusing lens focuses a linearly polarised plane light beam at the back focal plane (BFP) of an MO (MO₂) with high NA. The output beam collimated by MO₂ illuminates the SPR configuration created with a coverslip deposited with gold film. The *p*-polarised component excites SPR at a certain angle θ . The *s*-polarised component cannot excite SPR. By moving the BS horizontally, the focal position d of the incident beam on the BFP is changed and the incident angle θ can be adjusted accordingly. The incident angle is determined by

the sine relationship of an aplanatic imaging system, $d = f \sin \theta$ (f is the focal length of MO₂). The reflected light carrying the object information is recorded by the CCD camera after passing through the imaging lens (IL).

The bottom inset of Fig. 14a displays the off-axis hologram-recording process. The reflected beam from MO₂ is split into two orthogonally polarised components by a WP. The *p*-polarised component acts as the object beam carrying the SPR information of the sample. The *s*-polarised component acts as the reference beam carrying no sample information. The two interference beams possess the same polarisation state after passing through a polariser P and then interfere with each other. The approach of generating the uniform reference beam is different from the previously discussed common-path configurations. Compared with the lateral shearing-based type, the effective FOV of this setup is maintained without loss. Moreover, the level of common-path is greater than that of the point diffraction-based type.

Using the MO-coupling SPRHM setup in Fig. 14a, amplitude- and phase-contrast SPR images with high spatial resolution can be simultaneously obtained, by which the thin film thickness and refractive index distributions can be mapped unambiguously. Moreover, owing to the high temporal stability, this common-path SPRHM setup can be widely applied for dynamically measuring the small variations of refractive index or thickness. For example, we have measured the thickness of multilayer graphene film located in the near field of a metal surface⁹⁸. The measurement resolution can achieve sub-nanometre levels.

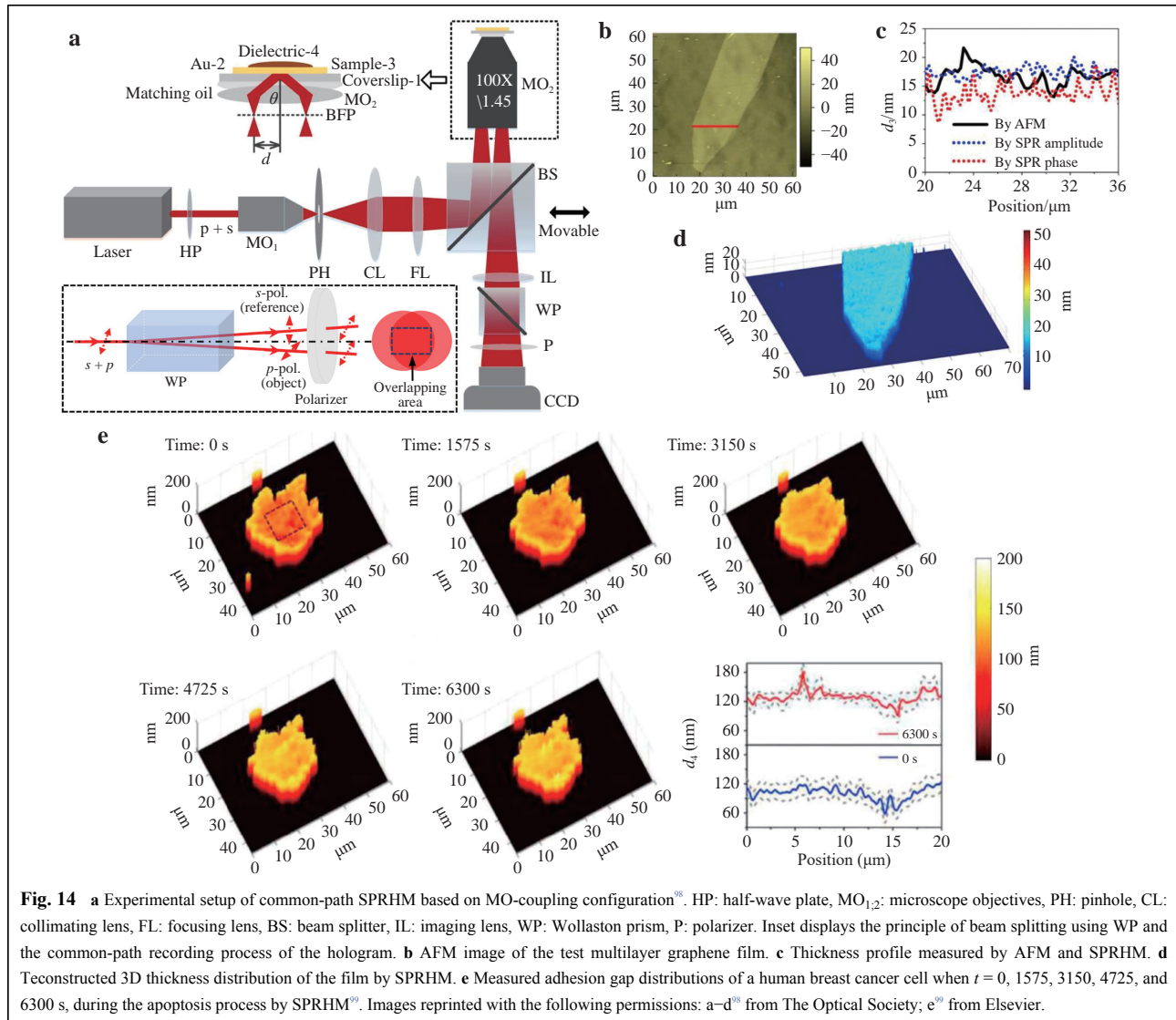


Fig. 14b–d display the experiment results. Furthermore, we also measured the adhesion gap distributions of human breast cancer cells during the apoptosis process in a dynamic and label-free manner (Fig. 14e)⁹⁹.

Discussion and outlook

We reviewed common-path configuration designs that aim to improve the temporal stability of off-axis holographic experimental setups. The common-path models were categorised into lateral shearing, point diffraction and other types. For each type, the design principle was given and the related techniques were summarised. For the lateral shearing-based type, the beam carrying the object information is first doubled using a glass plate, grating, or BS. Then, the portions of the two beams with and without the sample information create the shearing interference. This type has a simpler and more

compact design compared with that of other types. However, it requires an undisturbed portion of the illumination beam to generate the reference beam, which could reduce the FOV. Moreover, it has the potential problem of a duplicated image appearing on the camera target. This type is typically applied to spatially sparse samples. Conversely, the point diffraction-based type creates a uniform reference beam from the object beam by low-pass filtering in the Fourier domain. This type does not have the problems of duplicated image and limited FOV. However, it typically has a complex configuration and the two beams are separated at the spatial filtering position, resulting in a low level of common-path. This type is suitable for measuring small samples with high spatial frequency, as it is easy to generate the uniform reference beam by spatial filtering. Finally, other advanced designs such as using folding mirrors, specially positioned BS

Table 1 Comparison of three types of common-path configurations

Type	Advantages	Disadvantages	Applications
Lateral shearing	■ Simple & compact configuration	■ Limited FOV ■ Duplicated image (potential)	■ Spatially sparse samples
Point diffraction	■ Large FOV	■ Complex configuration ■ Low level of common-path	■ Small samples with high spatial frequency
Others	Specific design dependent		

cubes, and WPs were introduced. These designs could avoid the disadvantages existing in the former two types. For clarification, we summarise the advantages and disadvantages of the three types of common-path configurations in Table 1.

The critical point for each type is to allow the object and reference beams to propagate along the same or similar optical paths. The greater the level of similarity, the better the temporal stability the setup can possess. It is worth noting that each design has its own characteristics based on the properties of the measured sample and application environment. The majority of the current common-path designs are limited to a small number of application scenarios. Therefore, boosting the applications of common-path off-axis holographic configurations is an important research direction for the future. Moreover, combining this with other imaging techniques and achieving more functionality by common-path digital holography will attract tremendous interest from different fields.

Furthermore, the reviewed common-path configurations typically include fewer optical components than traditional interferometers. Therefore, the common-path configuration is the best choice in manufacturing compact and highly stable off-axis holographic instruments. From the viewpoint of instrument investigation, it is better to design common-path interference modules that can be easily integrated with commercial setups. In this manner, significant cost and time could be saved in developing commercial instruments. The instrumentation of common-path digital holography will lead to new interdisciplinary research directions in the fields of optical, electronic, and mechanical engineering. Owing to the high stability of the common-path holographic instruments, they can be used out of the laboratories and should find wide applications in industry, chemical, biomedicine, and other fields.

Acknowledgements

Support from the National Natural Science Foundation of China (NSFC) (61927810, 62075183, 62005219) and Fundamental Research Funds for the Central Universities (310202011qd004) is acknowledged.

Author contributions

J. Zhao supervised the project. J. Zhang, C. Ma, and T. Xi performed the

literature research. J. Zhang wrote the initial manuscript. S. Dai, C. Ma, J. Di, and J. Zhao revised and commented on the manuscript.

Conflict of interest

The authors declare no conflicts of interest.

Received: 08 March 2021 Revised: 10 August 2021 Accepted: 12 August 2021

Accepted article preview online: 13 August 2021

Published online: 15 September 2021

References

- Gabor, D. A new microscopic principle. *Nature* **161**, 777-778 (1948).
- Leith, E. N. & Upatnieks, J. Wavefront reconstruction with diffused illumination and three-dimensional objects. *Journal of the Optical Society of America* **54**, 1295-1301 (1964).
- Goodman, J. W. & Lawrence, R. W. Digital image formation from electronically detected holograms. *Applied Physics Letters* **11**, 77-79 (1967).
- Schnars, U. & Jüptner, W. Direct recording of holograms by a CCD target and numerical reconstruction. *Applied Optics* **33**, 179-181 (1994).
- Di, J. L. et al. Phase aberration compensation of digital holographic microscopy based on least squares surface fitting. *Optics Communications* **282**, 3873-3877 (2009).
- Di, J. L. et al. Reconstruction of axisymmetric liquid flow field in digital holographic interferometry. *Digital Holography 3D Imag. Mtg.*, 2015, doi: 10.1364/DH.2015.DTh2A.3.
- Sun, W. W. et al. Real-time visualization of Karman vortex street in water flow field by using digital holography. *Optics Express* **17**, 20342-20348 (2009).
- Wu, B. J. et al. Visual investigation on the heat dissipation process of a heat sink by using digital holographic interferometry. *Journal of Applied Physics* **114**, 193103 (2013).
- Zhang, Y. Y. et al. Real-time monitoring of the solution concentration variation during the crystallization process of protein-lysozyme by using digital holographic interferometry. *Optics Express* **20**, 18415-18421 (2012).
- Wang, J. et al. Dynamically measuring unstable reaction-diffusion process by using digital holographic interferometry. *Optics and Lasers in Engineering* **57**, 1-5 (2014).
- Chen, X. et al. Measurement and reconstruction of three-dimensional configurations of specimen with tiny scattering based on digital holographic tomography. *Applied Optics* **53**, 4044-4048 (2014).
- Wang, J. et al. Visual measurement of the pulse laser ablation process on liquid surface by using digital holography. *Journal of Applied Physics* **115**, 173106 (2014).
- Rajput, S. K. et al. Sound wave detection by common-path digital holography. *Optics and Lasers in Engineering* **137**, 106331 (2021).
- Nguyen, T. H. et al. Gradient light interference microscopy for 3D imaging of unlabeled specimens. *Nature Communications* **8**, 210

- (2017).
15. Kim, T. et al. White-light diffraction tomography of unlabelled live cells. *Nature Photonics* **8**, 256-263 (2014).
 16. Grilli, S. et al. Whole optical wavefields reconstruction by Digital Holography. *Optics Express* **9**, 294-302 (2001).
 17. Park, Y., Depeursinge, C. & Popescu, G. Quantitative phase imaging in biomedicine. *Nature Photonics* **12**, 578-589 (2018).
 18. Merola, F. et al. Tomographic flow cytometry by digital holography. *Light: Science & Applications* **6**, e16241 (2017).
 19. Kumar, M. et al. Common-path multimodal three-dimensional fluorescence and phase imaging system. *Journal of Biomedical Optics* **25**, 03210 (2020).
 20. Abbe, E. Beiträge zur Theorie des Mikroskops und der mikroskopischen Wahrnehmung. *Archiv für Mikroskopische Anatomie* **9**, 413-468 (1873).
 21. Cotte, Y. et al. Marker-free phase nanoscopy. *Nature Photonics* **7**, 113-117 (2013).
 22. Simon, B. et al. Tomographic diffractive microscopy with isotropic resolution. *Optica* **4**, 460-463 (2017).
 23. Alexandrov, S. A. et al. Synthetic aperture Fourier holographic optical microscopy. *Physical Review Letters* **97**, 168102 (2006).
 24. Maire, G. et al. Experimental demonstration of quantitative imaging beyond abbe' s limit with optical diffraction tomography. *Physical Review Letters* **102**, 213905 (2009).
 25. Lai, X. J. et al. Coded aperture structured illumination digital holographic microscopy for superresolution imaging. *Optics Letters* **43**, 1143-1146 (2018).
 26. Choi, Y. et al. Synthetic aperture microscopy for high resolution imaging through a turbid medium. *Optics Letters* **36**, 4263-4265 (2011).
 27. Micó, V. et al. Resolution enhancement in quantitative phase microscopy. *Advances in Optics and Photonics* **11**, 135-214 (2019).
 28. Wu, Y. C. et al. Extended depth-of-field in holographic imaging using deep-learning-based autofocusing and phase recovery. *Optica* **5**, 704-710 (2018).
 29. Rivenson, Y. et al. Phase recovery and holographic image reconstruction using deep learning in neural networks. *Light: Science & Applications* **7**, 17141 (2018).
 30. Ren, Z. B., Xu, Z. M. & Lam, E. Y. M. End-to-end deep learning framework for digital holographic reconstruction. *Advanced Photonics* **1**, 016004 (2019).
 31. Wu, Y. C. et al. Deep learning enables high-throughput analysis of particle-aggregation-based biosensors imaged using holography. *ACS Photonics* **6**, 294-301 (2019).
 32. Ren, Z. B., Xu, Z. M. & Lam, E. Y. Learning-based nonparametric autofocusing for digital holography. *Optica* **5**, 337-344 (2018).
 33. Pinkard, H. et al. Deep learning for single-shot autofocus microscopy. *Optica* **6**, 794-797 (2019).
 34. Dardikman-Yoffe, G. et al. PhUn-Net: ready-to-use neural network for unwrapping quantitative phase images of biological cells. *Biomedical Optics Express* **11**, 1107-1121 (2020).
 35. Nguyen, T. et al. Automatic phase aberration compensation for digital holographic microscopy based on deep learning background detection. *Optics Express* **25**, 15043-15057 (2017).
 36. Jo, Y. et al. Holographic deep learning for rapid optical screening of anthrax spores. *Science Advances* **3**, e1700606 (2017).
 37. Li, Y. et al. Classification of cell morphology with quantitative phase microscopy and machine learning. *Optics Express* **28**, 23916-23927 (2020).
 38. Goswami, N. et al. Rapid SARS-CoV-2 detection and classification using phase imaging with computational specificity. *bioRxiv* (in the press), doi: [10.1101/2020.12.14.422601](https://doi.org/10.1101/2020.12.14.422601).
 39. Rosen, J. & Brooker, G. Digital spatially incoherent Fresnel holography. *Optics Letters* **32**, 912-914 (2007).
 40. Rosen, J. & Brooker, G. Non-scanning motionless fluorescence three-dimensional holographic microscopy. *Nature Photonics* **2**, 190-195 (2008).
 41. Kelner, R., Katz, B. & Rosen, J. Common path in-line holography using enhanced joint object reference digital interferometers. *Optics Express* **22**, 4995-5009 (2014).
 42. Yamaguchi, I. & Zhang, T. Phase-shifting digital holography. *Optics Letters* **22**, 1268-1270 (1997).
 43. Rodriguez-Zurita, G. et al. One-shot phase-shifting phase-grating interferometry with modulation of polarization: case of four interferograms. *Optics Express* **16**, 7806-7817 (2008).
 44. Gao, P. et al. Parallel two-step phase-shifting digital holography microscopy based on a grating pair. *Journal of the Optical Society of America A* **28**, 434-440 (2011).
 45. Lin, M. et al. Parallel phase-shifting digital holography with adaptive function using phase-mode spatial light modulator. *Applied Optics* **51**, 2633-2637 (2012).
 46. Shan, M. G. et al. Parallel two-step spatial carrier phase-shifting common-path interferometer with a Ronchi grating outside the Fourier plane. *Optics Express* **21**, 2126-2132 (2013).
 47. Anand, A., Chhaniwal, V. & Javidi, B. Tutorial: common path self-referencing digital holographic microscopy. *APL Photonics* **3**, 071101 (2018).
 48. Nehmetallah, G. & Banerjee, P. P. Applications of digital and analog holography in three-dimensional imaging. *Advances in Optics and Photonics* **4**, 472-553 (2012).
 49. Bates, W. J. A wavefront shearing interferometer. *Proceedings of the Physical Society* **59**, 940-950 (1947).
 50. Singh, A. S. G. et al. Lateral shearing digital holographic imaging of small biological specimens. *Optics Express* **20**, 23617-23622 (2012).
 51. Di, J. L. et al. Dual-wavelength common-path digital holographic microscopy for quantitative phase imaging based on lateral shearing interferometry. *Applied Optics* **55**, 7287-7293 (2016).
 52. Kim, B. M., Park, S. J. & Kim, E. S. Single-shot digital holographic microscopy with a modified lateral-shearing interferometer based on computational telecentricity. *Optics Express* **25**, 6151-6168 (2017).
 53. O' Connor, T., Doblas, A. & Javidi, B. Structured illumination in compact and field-portable 3D-printed shearing digital holographic microscopy for resolution enhancement. *Optics Letters* **44**, 2326-2329 (2019).
 54. Patorski, K., Zdańkowski, P. & Trusiak, M. Grating deployed total-shear 3-beam interference microscopy with reduced temporal coherence. *Optics Express* **28**, 6893-6908 (2020).
 55. Han, L. et al. Double-channel angular-multiplexing polarization holography with common-path and off-axis configuration. *Optics Express* **25**, 21877-21886 (2017).
 56. Primot, J. & Guérineau, N. Extended Hartmann test based on the pseudoguiding property of a Hartmann mask completed by a phase chessboard. *Applied Optics* **39**, 5715-5720 (2000).
 57. Hillman, T. R. et al. Near-common-path self-reference quantitative phase microscopy. *IEEE Photonics Technology Letters* **24**, 1812-1814 (2012).
 58. Guo, R. L. et al. Quantitative phase imaging by wide-field interferometry with variable shearing distance uncoupled from the off-axis angle. *Optics Express* **28**, 5617-5628 (2020).
 59. Schubert, R. et al. Enhanced quantitative phase imaging in self-interference digital holographic microscopy using an electrically focus tunable lens. *Biomedical Optics Express* **5**, 4213-4222 (2014).
 60. Ma, C. J. et al. Lateral shearing common-path digital holographic microscopy based on a slightly trapezoid Sagnac interferometer. *Optics Express* **25**, 13659-13667 (2017).
 61. Varghese, A., Das, B. & Singh, R. K. Highly stable lens-less digital

- holography using cyclic lateral shearing interferometer and residual decollimated beam. *Optics Communications* **422**, 3-7 (2018).
62. Sun, T. F. et al. Single-shot two-channel Fresnel bimirror interferometric microscopy for quantitative phase imaging of biological cell. *Optics Communications*. **426**, 77-83 (2018).
 63. Edwards, C. et al. Measuring the nonuniform evaporation dynamics of sprayed sessile microdroplets with quantitative phase imaging. *Langmuir* **31**, 11020-11032 (2015).
 64. Di, J. L. et al. Quantitative and dynamic phase imaging of biological cells by the use of the digital holographic microscopy based on a beam displacer unit. *IEEE Photonics Journal* **10**, 6900510 (2018).
 65. Lee, K. & Park, Y. Quantitative phase imaging unit. *Optics Letters* **39**, 3630-3633 (2014).
 66. Kim, K. et al. Diffraction optical tomography using a quantitative phase imaging unit. *Optics Letters* **39**, 6935-6938 (2014).
 67. Serabyn, E. et al. Compact, lensless digital holographic microscope for remote microbiology. *Optics Express* **24**, 28540-28548 (2016).
 68. Ebrahimi, S. et al. Stable and simple quantitative phase-contrast imaging by Fresnel biprism. *Applied Physics Letters* **112**, 113701 (2018).
 69. Popescu, G. et al. Diffraction phase microscopy for quantifying cell structure and dynamics. *Optics Letters* **31**, 775-777 (2006).
 70. Girshovitz, P. & Shaked, N. T. Doubling the field of view in off-axis low-coherence interferometric imaging. *Light: Science & Applications* **3**, e151 (2014).
 71. Blum, O. & Shaked, N. T. Prediction of photothermal phase signatures from arbitrary plasmonic nanoparticles and experimental verification. *Light: Science & Applications* **4**, e322 (2015).
 72. Kumar, M. et al. Single-shot common-path off-axis dual-wavelength digital holographic microscopy. *Applied Optics* **59**, 7144-7152 (2020).
 73. Shaked, N. T. Quantitative phase microscopy of biological samples using a portable interferometer. *Optics Letters* **37**, 2016-2018 (2012).
 74. Mahajan, S. et al. Highly stable digital holographic microscope using Sagnac interferometer. *Optics Letters* **40**, 3743-3746 (2015).
 75. Singh, V., Tayal, S. & Mehta, D. S. Highly stable wide-field common path digital holographic microscope based on a Fresnel biprism interferometer. *OSA Continuum* **1**, 48-55 (2018).
 76. Zheng, C. et al. Digital micromirror device-based common-path quantitative phase imaging. *Optics Letters* **42**, 1448-1451 (2017).
 77. Vora, P. et al. Wide field of view common-path lateral-shearing digital holographic interference microscope. *Journal of Biomedical Optics* **22**, 126001 (2017).
 78. Edwards, C. et al. Diffraction phase microscopy: monitoring nanoscale dynamics in materials science [Invited]. *Applied Optics* **53**, G33-G43 (2014).
 79. Edwards, C. et al. Optically monitoring and controlling nanoscale topography during semiconductor etching. *Light: Science & Applications* **1**, e30 (2012).
 80. Edwards, C. et al. Digital projection photochemical etching defines gray-scale features. *Optics Express* **21**, 13547-13554 (2013).
 81. Bhaduri, B. et al. Diffraction phase microscopy with white light. *Optics Letters* **37**, 1094-1096 (2012).
 82. Pham, H. V. et al. Fast phase reconstruction in white light diffraction phase microscopy. *Applied Optics* **52**, A97-A101 (2013).
 83. Zheng, C. et al. Diffraction phase microscopy realized with an automatic digital pinhole. *Optics Communications* **404**, 5-10 (2017).
 84. Bhaduri, B. et al. Diffraction phase microscopy: principles and applications in materials and life sciences. *Advances in Optics and Photonics* **6**, 57-119 (2014).
 85. Hu, C. F. et al. Endoscopic diffraction phase microscopy. *Optics Letters* **43**, 3373-3376 (2018).
 86. Cardenas, N. & Mohanty, S. Decoupling of geometric thickness and refractive index in quantitative phase microscopy. *Optics Letters* **38**, 1007-1009 (2013).
 87. Rappaz, B. et al. Simultaneous cell morphometry and refractive index measurement with dual-wavelength digital holographic microscopy and dye-enhanced dispersion of perfusion medium. *Optics Letters* **33**, 744-746 (2008).
 88. Park, Y. et al. Spectroscopic phase microscopy for quantifying hemoglobin concentrations in intact red blood cells. *Optics Letters* **34**, 3668-3670 (2009).
 89. Fu, D. et al. Quantitative dispersion microscopy. *Biomedical Optics Express* **1**, 347-353 (2010).
 90. Pham, H. et al. Spectroscopic diffraction phase microscopy. *Optics Letters* **37**, 3438-3440 (2012).
 91. Lee, B. et al. Single grating reflective digital holography with double field of view. *IEEE Transactions on Industrial Informatics* **15**, 6155-6161 (2019).
 92. Chhaniwal, V. et al. Quantitative phase-contrast imaging with compact digital holographic microscope employing Lloyd's mirror. *Optics Letters* **37**, 5127-5129 (2012).
 93. Wang, D. Y. et al. Continuous-wave terahertz self-referencing digital holography based on Fresnel's mirrors. *Optics Letters* **45**, 913-916 (2020).
 94. Zhang, J. W. et al. Common-path digital holographic microscopy for near-field phase imaging based on surface plasmon resonance. *Applied Optics* **56**, 3223-3228 (2017).
 95. Zhang, J. W. et al. Wavelength-multiplexing surface plasmon holographic microscopy. *Optics Express* **26**, 13549-13560 (2018).
 96. Qu, W. J. et al. Transmission digital holographic microscopy based on a beam-splitter cube interferometer. *Applied Optics* **48**, 2778-2783 (2009).
 97. Zhang, J. W. et al. Dynamical measurement of refractive index distribution using digital holographic interferometry based on total internal reflection. *Optics Express* **23**, 27328-27334 (2015).
 98. Zhang, J. W. et al. Compact surface plasmon holographic microscopy for near-field film mapping. *Optics Letters* **42**, 3462-3465 (2017).
 99. Dai, S. Q. et al. Real-time and wide-field mapping of cell-substrate adhesion gap and its evolution via surface plasmon resonance holographic microscopy. *Biosensors and Bioelectronics* **174**, 112826 (2021).